



# CHORUS

This is the accepted manuscript made available via CHORUS. The article has been published as:

## Convert Acoustic Resonances to Orbital Angular Momentum

Xue Jiang, Yong Li, Bin Liang, Jian-chun Cheng, and Likun Zhang

Phys. Rev. Lett. **117**, 034301 — Published 12 July 2016

DOI: [10.1103/PhysRevLett.117.034301](https://doi.org/10.1103/PhysRevLett.117.034301)

# Convert acoustic resonances to orbital angular momentum

Xue Jiang,<sup>1</sup> Yong Li,<sup>2</sup> Bin Liang,<sup>1,\*</sup> Jian-chun Cheng,<sup>1,†</sup> and Likun Zhang<sup>3,‡</sup>

<sup>1</sup>*Collaborative Innovation Center of Advanced Microstructures and Key Laboratory of Modern Acoustics, MOE, Institute of Acoustics, Department of Physics, Nanjing University, Nanjing 210093, P. R. China*

<sup>2</sup>*CNRS, Institut Jean Lamour, Vandœuvre-lès-Nancy F-54506, France and Université de Lorraine, Institut Jean Lamour, Boulevard des Aiguillettes, BP: 70239, Vandœuvre-lès-Nancy 54506, France*

<sup>3</sup>*Department of Physics and Center for Nonlinear Dynamics, University of Texas at Austin, Austin, Texas 78712, USA*

(Dated: June 13, 2016)

We use acoustic resonances in a planar layer of a half-wavelength thickness to twist wave vectors of an in-coming plane wave into a spiral phase dislocation of an out-going vortex beam with orbital angular momentum (OAM). The mechanism is numerically and experimentally demonstrated by producing an airborne Bessel-like vortex beam. Our acoustic resonance-based OAM production differs from existing means for OAM production by enormous phased spiral sources or by elaborate spiral profiles. Our study can advance the capability of generating phase dislocated wave fields for further applications of acoustic OAM.

PACS numbers: XX

Wave fields with spiral phase dislocations [1] carry orbital angular momentum (OAM) such as for sound fields [2], optical waves [3], and electron beams [4]. A spiral phase  $\exp(im\theta)$  linearly proportional to the azimuth angle  $\theta$  is associated with a null field at the core. The carried OAM is discretized with the integer  $m$  (topological charge or order of the beam) to have an OAM-to-energy ratio  $m/\omega$  (where  $\omega$  is the radian frequency) for both quantum [3, 4] and classical waves [5, 6]. Transfer of the OAM to matters produces a torque associated with the transfer of wave energy such as in optical [7–9] and acoustic waves [10–14].

Acoustic waves with spiral phases and OAM of useful properties (e.g., [15–19]) were generated by *phased* spiral sources or *physically* spiral sources. A *phased* spiral source consists of an array of individually addressed transducers excited with appropriate screw phases to produce the expected phase profile in acoustic vortex beams [2, 20] or vortices of surface waves [21, 22]. A *physically* spiral source is a passive structure with screw dislocated profiles to produce phase profiles in wave fields, e.g., a helical substrate underneath ferroelectric film for airborne ultrasonic vortex generation [23], an absorbing surface with helix dimension for optoacoustic generation of a helical ultrasonic beam [24], a spiral-shaped object (spiral phase plate) for chiral scattering [25], and spiral gratings for diffracting waves into stable vortex beams [26].

The general principle for producing the spiral phase (denoted by  $\phi_{\text{out}}$ ) can be written as,

$$\phi_{\text{out}}(\theta) = \phi_{\text{in}} + k^{\text{eff}}l, \quad (1)$$

where the dependence of  $\phi_{\text{out}}$  on the azimuth angle  $\theta$  was produced via a  $\theta$ -dependent phase  $\phi_{\text{in}}$  in *phased*

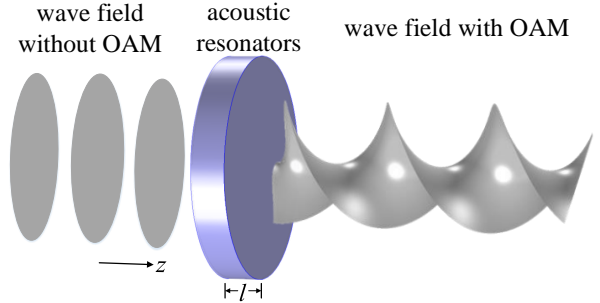


FIG. 1. Illustration of a resonant planar layer (blue) converting an in-coming axisymmetric wave without orbital angular momentum (OAM) to an out-going beam with helical wave front carrying OAM (wave fronts are shown in grey).

spiral sources or via a  $\theta$ -dependent propagation distance  $l$  through *physically* spiral sources.

The OAM production in this study doesn't have to rely on the  $\theta$  dependence in either phase  $\phi_{\text{in}}$  or propagation distance  $l$  in Eq. (1). Instead we produce a  $\theta$ -dependent effective wave number  $k^{\text{eff}}$ . The mechanism is that, regardless of *no*  $\theta$ -dependence in phase  $\phi_{\text{in}}$  of an axisymmetric in-coming wave and in propagation distance  $l$  of a planar layer [Fig. 1], acoustic resonances are excited in the layer to eventually produce the desired wave number  $k^{\text{eff}}$  for twisting the wave vectors into a phase dislocation of a vortex beam with OAM. We numerically model and experimentally demonstrate this mechanism by generating a Bessel-like vortex beam.

*Model.* — We construct the planar layer as an assembly of eight fan-like sections of resonators over the whole azimuth [Fig. 2(a)]. This amount of sections gives a reasonably good resolution for generating a vortex beam with a topological charge  $m = 1$ , as will

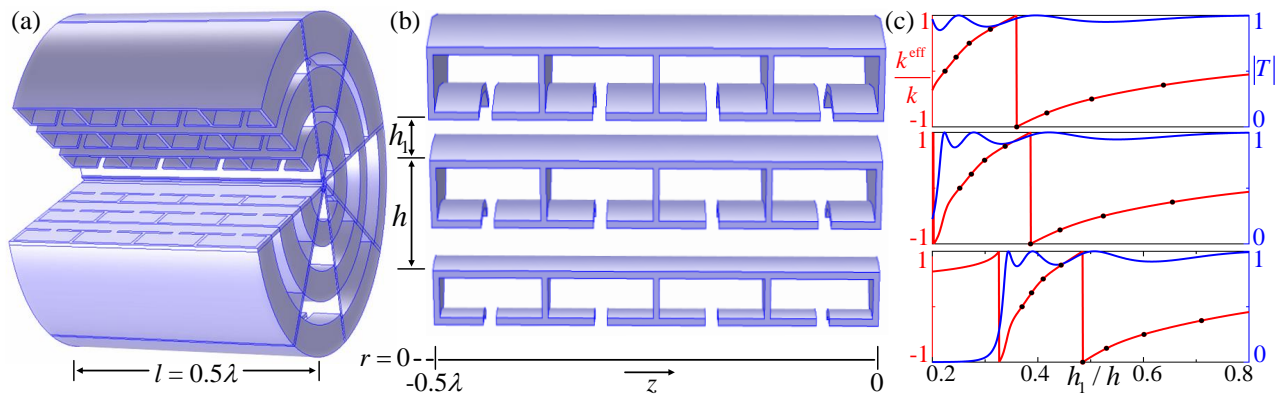


FIG. 2. (a) Schematic of the assembled layer consisting of eight fan-like sections of resonators. (b) An individual section consisting of three rows of resonators in the radial  $r$  direction (the radial resolution  $h = 0.1\lambda$  with  $\lambda$  being the sound wavelength), sided by pipes of varying height  $h_1$  to produce needed effective wave number [cf. Eq. (1)]; the thickness of the walls is  $0.01\lambda$ . (c) The effective wave number  $k^{\text{eff}}$  (red; normalized by  $k = 2\pi/\lambda$ ) and transmission coefficient  $|T|$  (blue) as functions of the height ratio  $h_1/h$  simulated for the three rows in (b), where in each case the eight black dots are parameters selected for the eight sections in (a) with equally discrete wave numbers to generate a first-order vortex beam. The averaged transmission efficiency of these  $8 \times 3$  elements is  $|T| = 95.1\% \pm 3.8\%$ .

72 be demonstrated via both numerical simulations and  
 73 experimental measurements. For generating higher-order  
 74 vortex beams, the amount of sections in the resonant  
 75 layer can be increased for a finer resolution.

76 Each individual section [Fig. 2(b)] is configured to  
 77 compose of three rows of resonators in the radius  
 78 (more rows can be employed for a larger radius).  
 79 Each row consists of four Helmholtz cavities and a  
 80 straight pipe [27]: (I) the series connection of four  
 81 cavities acting as lumped elements is for a fully flexible  
 82 manipulation of wave numbers  $k^{\text{eff}}$  (or phases), (II)  
 83 the combination of cavities and pipes provides hybrid  
 84 resonances that overcome the impedance mismatch  
 85 between the resonators and the surrounding air for a high  
 86 transmission, and (III) the layer is optimized to have  
 87 a propagation distance  $l = 0.5\lambda$ , a value that is small  
 88 enough to maintain hybrid resonances, but large enough  
 89 for negligible viscous effects (with the width of each  
 90 cavity's neck in air fixed at  $0.025\lambda$ ) and for manipulating  
 91 the wave number  $k^{\text{eff}}$  over a fully desired range (a  
 92 reasonably good performance can still be obtained with  
 93  $l \gtrsim 0.4\lambda$ ; c.f. Fig. 3 in [27]).

94 We use the resonant layer to produce desired spiral  
 95 phases and OAM by manipulating the  $k^{\text{eff}}$  for an  
 96 azimuthal dependence via tuning the height of the  
 97 cavities into an azimuthal dependence. The  $k^{\text{eff}}$  values  
 98 are modulated for the eight sections individually, denoted  
 99 by  $k_j^{\text{eff}}$  ( $j = 1, 2, \dots, 8$ ). Consider generating a first-order  
 100  $m = 1$  vortex beam, the  $k_j^{\text{eff}}$  values selected for the  
 101 eight sections cover the whole range from  $-k$  to  $k$  with a  
 102 step of  $k/4$  (where  $k = 2\pi/\lambda$  is the wave number in the  
 103 surrounding medium). If the three rows of resonators  
 104 have an identical transmission, the out-going normalized

105 field from an individual segment is approximated by:

$$106 \quad p|_{z=0} = \exp(ik_j^{\text{eff}}l - i\omega t) \text{ for } (j-1)\pi/4 < \theta < j\pi/4. \quad (2)$$

107 The out-going wave propagates in a rigid cylindrical  
 108 waveguide of radius  $a$  as for generating a vortex beam of  
 109 a Bessel-like profile. The wave can be represented as a  
 110 sum of cylindrical Bessel modes:

$$111 \quad p = \sum_m \sum_n A_{m,n} J_m(k_{m,n}r) \exp(ik_z z + im\theta - i\omega t), \quad (3)$$

112 where  $A_{m,n}$  is the modal amplitude,  $J_m(k_{m,n}r)$  is the  
 113  $m$ -order Bessel function,  $k_{m,n}$  is the  $n$ -th positive root of  
 114 equation  $\partial J_m(k_{m,n}r)/\partial(k_{m,n}r)|_{r=a} = 0$ , and the axial  
 115 wave number is  $k_z = \sqrt{k^2 - k_{m,n}^2}$ . We restrict the  
 116  $(m, n) = (1, 1)$  mode as the only propagating vortex  
 117 mode in the waveguide by choosing  $k$  to be higher than  
 118 the critical wave number of the  $(1, 1)$  mode (i.e.  $k_{1,1}$ )  
 119 but lower than that of  $(1, 2)$  mode (i.e.  $k_{1,2}$ ). Given the  
 120 condition at  $z = 0$  in Eq. (2), the normalized propagating  
 121 field would be:

$$122 \quad p = J_1(k_{1,1}r) \exp(ik_z z + i\theta - i\omega t) \quad (4)$$

123 which is exactly a first-order Bessel-like vortex beam  
 124 (topological charge  $m = 1$ ) that carries OAM.

125 *Simulations and Measurements.* — Now we simulate  
 126 the conversion of the acoustic resonances to OAM with  
 127 finite element method based on COMSOL Multiphysics  
 128 software (with the Pressure Acoustic Interface [28]).  
 129 The simulations resemble the experimental setup of an  
 130 in-coming wave at 2287 Hz (with an airborne wavelength  
 131 of 15 cm), simulated as a plane wave to propagate along  
 132 an air-filled cylindrical waveguide of a 5-cm radius and  
 133 transmit through a coaxial resonant layer of a 7.5-cm

134 thickness. The airborne sound wave number  $k = 41.9$   
 135 rad/s is in between the values of  $k_{1,1} = 36.8$  rad/s  
 136 and  $k_{1,2} = 106.4$  rad/s of the waveguide, satisfying  
 137 the criteria stated in aforementioned model analysis.  
 138 Solid materials (used in experiments) for the waveguide  
 139 (PMMA) and for the layer (UV resin) are treated as  
 140 acoustically rigid in simulations because of the strong  
 141 contrast of acoustic impedance between these materials  
 142 and air [29].

143 Simulations individually for the three rows in Fig. 2(b)  
 144 (via two-dimensional axisymmetric simulations) indicate  
 145 an almost unity transmission  $|T|$  over a wide range of  
 146 height ratio  $h_1/h$  [Fig. 2(c), blue curves], guaranteeing  
 147 the efficient conversion of acoustic resonances to OAM.  
 148 The effective wave number  $k^{\text{eff}}$ , calculated from  $\arg(T)/l$ ,  
 149 exhibits the required coverage of full  $2k$  range [Fig. 2(c),  
 150 red curves], where the eight dots give the eight discrete  
 151  $k_j^{\text{eff}}$  values for the eight sections in Fig. 2(a). Their  
 152 transmissions have an average of  $95.1\% \pm 3.8\%$ .

153 The simulated transmission through the whole layer  
 154 (via three-dimensional simulations in the air-filled  
 155 waveguide) exhibits an expected twisted wave front with  
 156 a screw dislocation along the propagation axis [Fig. 3(a)].  
 157 Distribution of phases and sound amplitudes at four  
 158 cross sections [Fig. 3(b)] illustrates a transition from  
 159 near to far field. The transition point would be around  
 160  $a^2/\lambda = 0.11\lambda$ , estimated from radiation of circular piston  
 161 [30]. The distortion in both phases and amplitudes is  
 162 obvious at the cross section  $z = 0.01\lambda$  [left hand side  
 163 panels in Fig. 3(b)], while at the rest of three cross  
 164 sections  $z \geq 0.11\lambda$  the phase regularly jumps  $2\pi$  over one  
 165 annular loop, revealing the expected topological charge  
 166  $m = 1$ . Another representative characteristic of the  
 167 Bessel-like vortex – null pressure amplitude at the core  
 168 – is also clearly shown in Fig. 3(b) (bottom), where a  
 169 small asymmetry over the azimuth is due to the small  
 170 differences of transmission  $|T|$  among the resonators  
 171 [Fig. 2(c)]. The overall transmission efficiency through  
 172 the layer is 93.8% when calculated from squared root of  
 173 out-going to in-coming sound power ratio.

174 Experiments to verify and demonstrate the OAM  
 175 production are conducted in a 300-cm long waveguide  
 176 and using a layer fabricated via 3D printing technology  
 177 [Fig. 4(a) [31]]. A monochromatic sound, excited  
 178 by a loudspeaker (4-inch diameter) facing into the  
 179 waveguide at one end, propagates as a plane wave  
 180 through the waveguide and illuminate on the layer placed  
 181 at the middle of the waveguide. Transmitted sound  
 182 is absorbed by sound absorbing foam at the other end  
 183 of the waveguide. Three-dimensional sound field scan  
 184 is conducted by employing two microphones (1/4-inch,  
 185 Brüel & Kæjr type-4961) with a mobile one scanning  
 186 the out-going field with OAM and a fixed one detecting  
 187 the in-coming wave as a reference signal. Phase and  
 188 amplitude of sound in each scan point are retrieved from  
 189 cross-spectrum of the two signals.

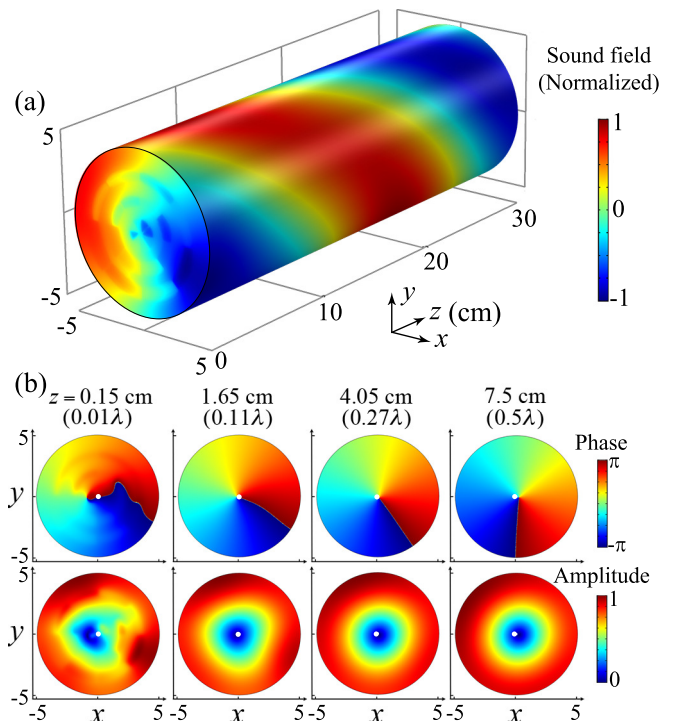


FIG. 3. Numerical simulations. (a) Airborne sound pressure field on outgoing surface of the planar layer (located at  $-0.5\lambda \leq z \leq 0$ ) and inner surface of a cylindrical waveguide of a 5-cm radius. (b) Phase (top) and amplitude (bottom) of the field at four cross sections, illustrating the transition from near- to far-field, where the geometric centers of the cross sections are denoted by the white dots. The simulations are for sound of a frequency 2287 Hz ( $\lambda = 15$  cm in air).

190 The measured phase distributions at far-field cross  
 191 sections  $z = 0.27\lambda$  and  $0.5\lambda$  [Fig. 4(b)] recover  
 192 the corresponding simulated results in a good shape  
 193 [Fig. 3(b)]. The phase profile is measured (via cross  
 194 correlation) to rotate an angle of  $0.217\pi$  radians between  
 195 these two cross sections, revealing an axial wave number  
 196  $k_z = 19.8$  rad/m (given the known propagation distance  
 197 of  $0.23\lambda$  in between), verifying a value of  $k_z =$   
 198  $\sqrt{k^2 - k_{m,n}^2} = 20$  rad/m calculated from the known  
 199 frequency and cylinder geometry.

200 The corresponding sound amplitude measured at the  
 201 two far-field cross sections is shown in Fig. 4(c) for a  
 202 direct comparison with simulated results and theoretical  
 203 profiles  $J_1(k_{1,1}r)$  [cf. Eq. (3)]. The results show the  
 204 primary characteristics of the  $m = 1$  Bessel-like vortex in  
 205 the measured amplitude. The transmission (square root  
 206 of out-going to in-coming sound power ratio) is measured  
 207 to be 88.4% [32], verifying the high efficiency and  
 208 the effectiveness of the proposed scheme in converting  
 209 acoustic resonances to OAM.

210 The underlying mechanism on manipulating  $k^{\text{eff}}$  allows  
 211 for adjusting resonant frequencies and selecting the  
 212 propagating mode via tailoring structural parameters of



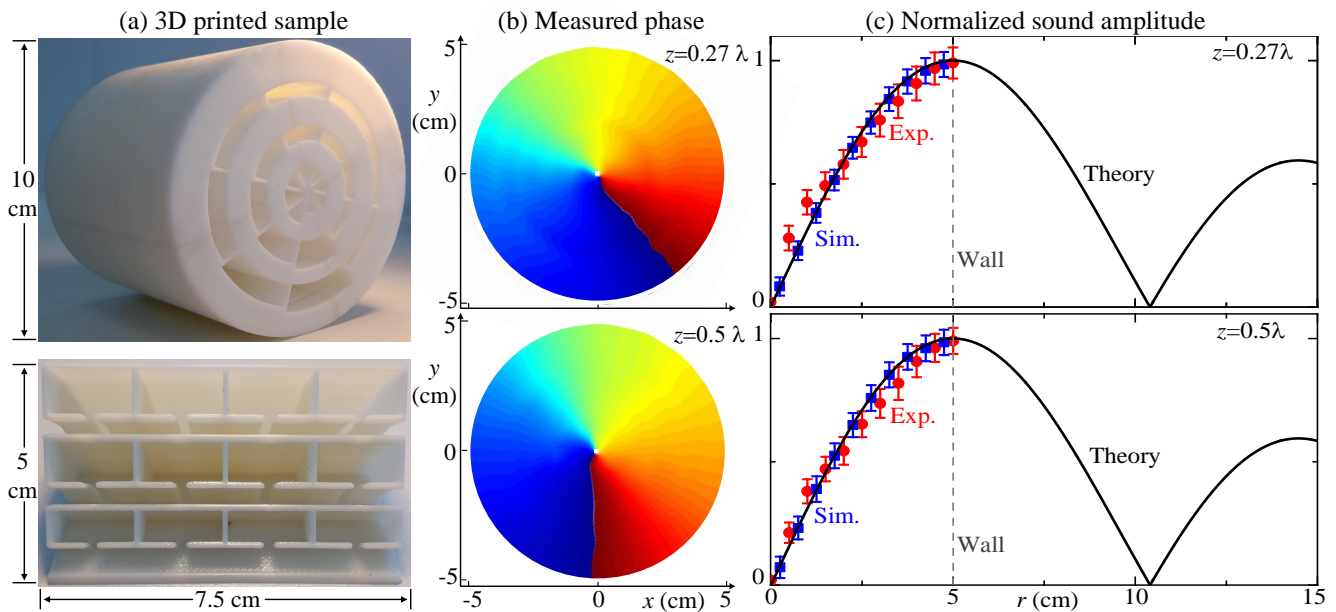


FIG. 4. Experiments. (a) The assembled sample (top) and its individual section (bottom), fabricated by 3D printing technology with UV resin, for generating a first-order Bessel-like vortex beam in experiments. (b) Phase distributions measured at  $z = 0.27\lambda$  (top) and  $0.5\lambda$  (bottom). (c) Measurements of sound pressure amplitudes (red) as functions of radius  $r$  at the same  $z$  as in (b) are compared with numerical simulations (blue) and theoretical Bessel profiles (black). The measurements are taken at every  $\pi/9$  in the azimuthal and every 0.5 cm in the radial. The measurements and simulations are shown in (c) as an average (dots) and uncertainty (error bars) over the azimuthal. The measured transmission at these two cross sections is 88.4%.

213 the resonators. A proper frequency range ensures the  
 214 conversion to the desired mode, chosen as the (1, 1) mode  
 215 in this study, while other modes completely fall in the  
 216 evanescent regime and are trapped in the near field.

217 *Discussions.* — We have used a resonant planar layer  
 218 to produce a new mechanism for generating acoustic  
 219 beams with OAM. Performance of the mechanism  
 220 was demonstrated by employing the resonant layer to  
 221 produce OAM of a first-order airborne vortex beam of  
 222 a smooth spiral phase and of a Bessel-like profile. In  
 223 comparison with existing ways for OAM production by  
 224 phased spiral sources that need sophisticated electronic  
 225 control and by physically spiral sources that need screw  
 226 profiles and may also have a bulky size, our acoustic  
 227 resonance-based OAM production via manipulating  
 228 effective wave numbers  $k^{\text{eff}}$  bears the advantages of high  
 229 efficiency, compact size and planar profile.

230 The conversion of OAM from fundamental phenomena  
 231 of acoustic resonances opens an avenue for producing  
 232 acoustic vortex beams with OAM and could promote  
 233 practical applications of the screw wave fields. Given  
 234 that the resonant planar layer employed here has a small  
 235 radius, the generated vortex beam would have a strong  
 236 divergence, but that divergence doesn't occur here for  
 237 propagation in a waveguide. A layer with a larger  
 238 radius though, with an increased number of resonators  
 239 in both the radial and azimuthal directions, can be  
 240 employed to generate a less diverging beam in free space  
 241 for applications in long range alignment [2], information

242 transmission [33], etc. The larger layer can even be used  
 243 to generate a focused vortex beam provided that both  
 244 the  $k^{\text{eff}}$  and transmission  $|T|$  have a desired dependence  
 245 on both the azimuth and radius by properly selecting  
 246 parameters of the resonators [Fig. 2(c)].

247 We may in principle extend the present mechanism  
 248 of producing OAM via acoustic resonance-based  
 249 manipulation of effective wave number  $k^{\text{eff}}$  to underwater  
 250 propagation, but that environment requires alternative  
 251 materials for a sufficient contrast of impedance with that  
 252 of water or alternative media for resonances in water  
 253 (e.g., soft media [34]).

254 X.J., B.L. and J.C. acknowledge support from National  
 255 Basic Research Program of China (973 Program; Grant  
 256 Nos. 2011CB707900 and 2012CB921504), Natural  
 257 Science Foundation of China (Grant Nos. 11174138,  
 258 11174139, 11222442, and 81127901), NCET-12-0254, and  
 259 a project funded by the Priority Academic Program  
 260 Development of Jiangsu Higher Education Institutions.  
 261 Y.L. acknowledges discussions with Dr. Badreddine  
 262 Assouar. L.Z. acknowledges support from ONR.  
 263 X.J. and Y.L. contribute equally to the paper.

\* liangbin@nju.edu.cn

† jccheng@nju.edu.cn

‡ lzhang@chaos.utexas.edu

- [1] J. F. Nye and M. V. Berry, “Dislocations in wave trains,” *Proc. R. Soc. A* **336**, 165 (1974).
- [2] Brian T. Hefner and Philip L. Marston, “An acoustical helicoidal wave transducer with applications for the alignment of ultrasonic and underwater systems,” *J. Acoust. Soc. Am.* **106**, 3313–3316 (1999).
- [3] L. Allen, M. W. Beijersbergen, R. J. C. Spreeuw, and J. P. Woerdman, “Orbital angular momentum of light and the transformation of laguerre-gaussian laser modes,” *Phys. Rev. A* **45**, 8185 (1992).
- [4] B. J. McMorran, A. Agrawal, I. M. Anderson, and A. A. Herzing, “Electron vortex beams with high quanta of orbital angular momentum,” *Science* **331**, 192 (2011).
- [5] L. K. Zhang and P. L. Marston, “Angular momentum flux of nonparaxial acoustic vortex beams and torques on axisymmetric objects,” *Phys. Rev. E* **84**, 065601 (2011).
- [6] C. E. M. Demore, Z. Yang, A. Volovick, S. Cochran, M. P. MacDonald, and G. C. Spalding, “Mechanical evidence of the orbital angular momentum to energy ratio of vortex beams,” *Phys. Rev. Lett.* **108**, 194301 (2012).
- [7] H. He, M. E. J. Friese, N. R. Heckenberg, and H. Rubinsztein-Dunlop, “Direct observation of transfer of angular momentum to absorptive particles from a laser beam with a phase singularity,” *Phys. Rev. Lett.* **75**, 826–829 (1995).
- [8] V. Garcés-Chávez, D. McGloin, M. J. Padgett, W. Dultz, H. Schmitzer, and K. Dholakia, “Observation of the transfer of the local angular momentum density of a multiringed light beam to an optically trapped particle,” *Phys. Rev. Lett.* **91**, 093602 (2003).
- [9] C. M. Herne, K. M. Capuzzi, E. Sobel, and R. T. Kropas, “Rotation of large asymmetrical absorbing objects by Laguerre-Gauss beams,” *Opt. Lett.* **40**, 4026–4029 (2015).
- [10] L. K. Zhang and P. L. Marston, “Acoustic radiation torque and the conservation of angular momentum (L),” *J. Acoust. Soc. Am.* **129**, 1679–1680 (2011).
- [11] L. K. Zhang and P. L. Marston, “Acoustic radiation torque on small objects in viscous fluids and connection with viscous dissipation,” *J. Acoust. Soc. Am.* **136**, 2917–2921 (2014).
- [12] Karen Volke-Sepúlveda, Arturo O. Santillán, and Ricardo R. Boullosa, “Transfer of angular momentum to matter from acoustical vortices in free space,” *Phys. Rev. Lett.* **100**, 024302 (2008).
- [13] A. Anhäuser, R. Wunenburger, and E. Brasselet, “Acoustic rotational manipulation using orbital angular momentum transfer,” *Phys. Rev. Lett.* **109**, 034301 (2012).
- [14] Z. Y. Hong, J. Zhang, and B. W. Drinkwater, “Observation of orbital angular momentum transfer from Bessel-shaped acoustic vortices to diphasic liquid-microparticle mixtures,” *Phys. Rev. Lett.* **114**, 214301 (2015).
- [15] J.-L. Thomas and R. Marchiano, “Pseudo angular momentum and topological charge conservation for nonlinear acoustical vortices,” *Phys. Rev. Lett.* **91**, 244302 (2003).
- [16] K. D. Skeldon, C. Wilson, M. Edgar, and M. J. Padgett, “An acoustic spanner and its associated rotational doppler shift,” *New J. Phys.* **10**, 013018 (2008).
- [17] S. T. Kang and C. K. Yeh, “Potential-well model in acoustic tweezers,” *IEEE. T. Ultrason. Ferr.* **57**, 1451–1459 (2010).
- [18] B. T. Hefner and B. R. Dzikowicz, “A spiral wave front beacon for underwater navigation: Basic concept and modeling,” *J. Acoust. Soc. Am.* **129**, 3630–3639 (2011).
- [19] Diego Baresch, Jean-Louis Thomas, and Régis Marchiano, “Observation of a single-beam gradient force acoustical trap for elastic particles: Acoustical tweezers,” *Phys. Rev. Lett.* **116**, 024301 (2016).
- [20] Régis Marchiano and Jean-Louis Thomas, “Synthesis and analysis of linear and nonlinear acoustical vortices,” *Phys. Rev. E* **71**, 066616 (2005).
- [21] A. Riaud, J.-L. Thomas, M. Baudoin, and O. Bou Matar, “Taming the degeneration of bessel beams at an anisotropic-isotropic interface: Toward three-dimensional control of confined vortical waves,” *Phys. Rev. E* **92**, 063201 (2015).
- [22] A. Riaud, J.-L. Thomas, E. Charron, A. Bussonnière, O. Bou Matar, and M. Baudoin, “Anisotropic swirling surface acoustic waves from inverse filtering for on-chip generation of acoustic vortices,” *Phys. Rev. Applied* **4**, 034004 (2015).
- [23] J. L. Ealo, J. C. Prieto, and F. Seco, “Airborne ultrasonic vortex generation using flexible ferroelectrets,” *IEEE. T. Ultrason. Ferr.* **58**, 1651–1657 (2011).
- [24] S. Gspan, A. Meyer, S. Bernet, and M. Ritsch-Marte, “Optoacoustic generation of a helicoidal ultrasonic beam,” *J. Acoust. Soc. Am.* **115**, 1142–1146 (2004).
- [25] R. Wunenburger, J. I. V. Lozano, and E. Brasselet, “Acoustic orbital angular momentum transfer to matter by chiral scattering,” *New J. Phys.* **17**, 103022 (2015).
- [26] X. Jiang, J. J. Zhao, S. L. Liu, B. Liang, X. Zou, J. Yang, C. Qiu, and J. C. Cheng, “Broadband and stable acoustic vortex emitter with multi-arm coiling slits,” *Appl. Phys. Lett.* **108**, 203501 (2016).
- [27] Y. Li, X. Jiang, B. Liang, J.-c. Cheng, and L. K. Zhang, “Metascreen-based acoustic passive phased array,” *Phys. Rev. Applied* **4**, 024003 (2015).
- [28] *Acoustics Module User’s Guide*, COMSOL Multiphysics  $\text{\textcircled{R}}$  v.5.2, COMSOL AB, Stockholm, Sweden (2015).
- [29] PMMA for the waveguide: density  $1220 \text{ kg/m}^3$  and sound speed  $3000 \text{ m/s}$ , UV resin for the layer:  $1400 \text{ kg/m}^3$  and  $1950 \text{ m/s}$ , in contrast with air:  $1.21 \text{ kg/m}^3$  and  $343 \text{ m/s}$ .
- [30] L. E. Kinsler, A. R. Frey, A. B. Coppens, and J. V. Sanders, *Fundermentals of Acoustics* (John Wiley & Sons, New York, 2000).
- [31] For the sake of convenient assemble and good sealing between the layer and waveguide, the fabricated sample has an addition of a central cylinder of 2-mm radius and an annulus of 3-mm thickness on the periphery.
- [32] The measured transmission with dissipation has a few percentage lower than simulated 93.8 %, due to viscous dissipation in measurements.
- [33] R. Marchiano and J.-L. Thomas, “Doing arithmetic with nonlinear acoustic vortices,” *Phys. Rev. Lett.* **101**, 064301 (2008).
- [34] T. Brunet, A. Merlin, B. Mascaró, K. Zimny, J. Leng, O. Poncelet, C. Aristégui, and O. Mondain-Monval, “Soft 3d acoustic metamaterial with negative index,” *Nature Mater.* **14**, 384 (2015).